

Short-Range Low-VHF Channel Characterization in Cluttered Environments

Fikadu T. Dagefu, *Member, IEEE*, Gunjan Verma, Chirag R. Rao, Paul L. Yu, *Member, IEEE*, Jonathan R. Fink, *Member, IEEE*, Brian M. Sadler, *Fellow, IEEE*, and Kamal Sarabandi, *Fellow, IEEE*

Abstract—The lower VHF band has potential for low-power, short-range communications, as well as for geolocation applications, in both indoor and urban environments. Most prior work at low VHF focuses on longer range path loss modeling, often with one node elevated. In this paper, we study indoor/outdoor near-ground scenarios through experiments and electromagnetic wave propagation simulations. These include the effects of indoor penetration through walls and obstacles, as well as indoor/outdoor cases, for both line of sight (LoS) and nonLoS (NLoS), at ranges up to 200 m. Mounting our receiver (Rx) on a robotic platform enabled the collection of thousands of measurements over an extended indoor/outdoor test area. We measure the channel transfer function, employing bandpass waveform sampling, with pulse and tone probe signals. Based on statistical tests, we show that the measured channels have a nearly ideal scalar attenuation and delay transfer function, with minimal phase distortion, and little to no evidence of multipath propagation. Compared with higher VHF and above, the measured short-range VHF channels do not exhibit small-scale fading, which simplifies communications Rx signal processing, and enables phase-based geolocation techniques.

Index Terms—Channel phase distortion, indoor/outdoor propagation measurements, lower VHF band, near-ground propagation, path loss, transfer function measurements, wireless channel characterization.

I. INTRODUCTION

RELIABLE wireless communication is of paramount importance for many important civilian and military applications. In challenging environments such as urban canyons and indoor settings, achieving a reliable communications link minimally impeded by scatterers is extremely challenging. In recent years, rapid global urbanization and the ever increasing need for reliable communications in emergency and tactical applications [1], [2] has necessitated reliable communications paradigms for such environments to support humans and autonomous agents, enabling communications, sensing, real-time positioning, and tracking [3], [4].

Manuscript received March 15, 2014; revised January 29, 2015; accepted March 25, 2015. Date of publication April 01, 2015; date of current version May 29, 2015.

F. T. Dagefu, G. Verma, C. R. Rao, P. L. Yu, J. R. Fink, and B. M. Sadler are with the Army Research Laboratory, Adelphi, MD 20783 USA (e-mail: fikadu.t.dagefu.ctr@mail.mil; gunjan.verma.civ@mail.mil; chirag.r.rao.civ@mail.mil; paul.l.yu.civ@mail.mil; jonathan.r.fink3.civ@mail.mil; brian.m.sadler6.civ@mail.mil).

K. Sarabandi is with the Department of Electrical Engineering and Computer Science, University of Michigan, Ann Arbor, MI 48109-2122 USA (e-mail: saraband@eecs.umich.edu).

Color versions of one or more of the figures in this paper are available online at <http://ieeexplore.ieee.org>.

Digital Object Identifier 10.1109/TAP.2015.2418346

State-of-the-art communication systems that operate in the upper VHF through microwave bands suffer from significant attenuation and small-scale fading, as well as phase distortion, caused by high levels of multipath [5], [6]. In a complex environment at these frequencies, without line of sight (LoS), multipath propagation is the dominant signal source between a transmitter (Tx) and a receiver (Rx), whereas the direct path signal is often extremely weak due to penetration loss. Major efforts have been devoted over many decades to design sophisticated multipath mitigation techniques, incorporating channel coding and modulation schemes [7]. Such schemes add significantly to transceiver hardware and software complexity, yet still may provide marginal performance in challenging scenarios, e.g., necessitating networking over many hops, or high-transmit power.

The lower VHF band has significant potential to support low complexity, low power, highly reliable communications. This stems from the fact that at lower VHF, scatterers are small in terms of wavelength [3], [8]. Consequently, strong penetration through multiple walls and buildings can be achieved at relatively low power. Reflection, scattering, and diffraction phenomena are dramatically reduced, yielding a short-range channel that is LoS-like in terms of very slight phase distortion and delay spread. This liberates the low-VHF system designer from the typically stringent requirements on power, system bandwidth, and complex equalization processing needed at other bands.

Conventional antennas such as dipoles operating in the lower VHF band are very large, limiting their practical application. However, due to recent advances in antenna miniaturization techniques and the development of palm-sized lower VHF antennas with good performance [9], [10], interest in low power, low data rate communications in this band is increasing. Thus, there is a need to better understand the channel characteristics in this band, to better inform and guide the design of systems. While the frequency allocations vary in different regions of the world, in North America, there is dual allocation at low VHF, consisting of primary and secondary allocations. Applications and users include the industrial, scientific, and medical (ISM) band, the U.S. Army Single Channel Ground and Airborne Radio System (SINCGARs), highway patrol radios, and ocean radars [11].

The large majority of channel characterization in complex propagation scenarios consist of path loss measurements in support of long-range commercial wireless applications which operate in the upper UHF and microwave range [12]. These studies typically assume a powerful base station with an

elevated antenna serving mobile units located near ground [1], as is common in cellular phone and other mobile communications. These classical empirically derived urban propagation models are not appropriate for near-ground nodes operating at the lower VHF and HF bands [16], [17].

Urban path-loss models in the upper VHF and military UHF bands based on field measurements have been presented in [1], [13]. Similar path-loss models in the lower VHF range have also been proposed [2], [14], [15]. In the literature, little attention has been paid to shorter range lower VHF band channel characterization for near-ground nodes deployed in complex propagation scenarios, especially for indoor-to-indoor and outdoor-to-indoor communications. We note that the majority of work regarding HF/VHF channel modeling focuses on long-range ionospheric and ground-wave propagation [20].

In this paper, we study near-ground, wireless channel in the lower VHF band for indoor and indoor/outdoor scenarios (with specific focus on channel phase distortion), drawing from extensive propagation measurements and simulations using a finite difference time domain (FDTD)-based electromagnetic model. In Section II, the full-wave electromagnetic simulation results are described. In Sections III and IV, we discuss the measurement system and scenarios, experimental results and analysis based on our measurements, including path-loss, small-scale fading, and phase distortion. We have also measured the bit error rate (BER) versus received signal-to-noise ratio (SNR) for QPSK transmission. Using only timing and carrier estimation at the Rx, the resulting BER curves coincide with theoretical additive white Gaussian noise (AWGN) channel BER predictions. Due to space limitations, BER results are not included here, but are available in [22].

II. MULTIPATH ANALYSIS AND FULL-WAVE SIMULATION

In this section, we consider the multipath channel and associated channel transfer function. This is a precursor to measuring and estimating the channel transfer function in amplitude and phase. An indoor/outdoor propagation simulation is used as an initial look at the problem (later, we consider a physical scene that is very similar to the simulation). These results set the stage for our experiments in the sections that follow, including statistical tests for the presence or absence of multipath, testing for an ideal transfer function, and communications BER performance without equalization.

Our simulation geometry is shown in Fig. 1. In the upper UHF to microwave bands, ray tracing approaches are often used to simulate wave propagation. Ray tracing is relatively straightforward and computationally tractable under the assumption that the size of the scatterers in the environment is generally much larger than the wavelength. However, this assumption breaks down in the lower VHF, where the size of some scatterers becomes comparable to the wavelength. For this reason, we resort to a technique that directly solves Maxwell's equations to characterize the wireless channel in the lower VHF band. In particular, we use EMCUBE, a commercial full-wave solver based on FDTD [21].

The simulation scene in Fig. 1 consists of several walls, floor, and ceiling, as well as doors and windows (the floor and ceiling

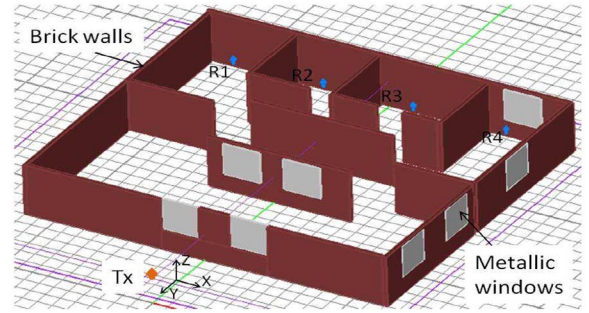


Fig. 1. FDTD simulation geometry used for short-range phase distortion analysis. The walls are modeled as homogeneous dielectric slabs and metal sheets are introduced to simulate a more realistic environment.

are not shown in the figure for clarity). The floor is modeled as a half-space homogeneous dielectric medium with a dielectric constant of concrete ($\epsilon_r = 4.5 + j0.011$). The walls are modeled as dielectric slabs with a dielectric constant of brick ($\epsilon_r = 4 + j0.001$). To make this indoor scenario more realistic, rectangular metal sheets ($1.2 \text{ m} \times 1.2 \text{ m}$) are included to simulate the effect of windows since the metal sheet has the same effect as having a metallic frame around the edges of the window due to the relatively large wavelength. The dimensions of the overall scenario are $15 \text{ m} \times 15 \text{ m}$ by 3.3 m . The geometry is kept relatively small to make the simulation more computationally tractable. A vertically polarized dipole antenna positioned outdoors is used as a Tx, emitting a Gaussian envelope pulse that is frequency translated to 40 MHz , with a 1 MHz bandwidth. Four vertically polarized Rx antennas are positioned indoors and the received signal from each antenna is recorded. Note that the Rx positions are symmetrically positioned on either side of the Tx antenna along the x -axis.

In addition to path-loss, we consider the phase coherence and memory in the channel. Denote the linear time invariant channel impulse response as $h(n) = \sum_{k=0}^{N-1} P_k e^{j\phi_k} \delta(n - n_k)$, where P_k and ϕ_k are the amplitude and phase of the k^{th} component of the signal. The $k = 0$ term corresponds to the first arrival in time, where we assume that $n_0 < n_1 < \dots < n_{N-1}$ model the delays of the N multipath components. Taking the Fourier transform, we can express the transfer function as

$$H(f) = P_0 e^{j\phi_0} e^{-j2\pi f n_0} + \sum_{k=1}^{N-1} P_k e^{j\phi_k} e^{-j2\pi f n_k} \quad (1)$$

where P_k and ϕ_k are the amplitude and phase of the k^{th} component of the Fourier transform of $h(n)$. The transfer function phase can be written as

$$\begin{aligned} \angle H(f) &= \tan^{-1} \left[\frac{P \sin(\phi_0 - 2\pi f n_0) + \sum_{k=1}^{N-1} P_k \sin(\phi_k - 2\pi f n_k)}{P \cos(\phi_0 - 2\pi f n_0) + \sum_{k=1}^{N-1} P_k \cos(\phi_k - 2\pi f n_k)} \right] \\ & \quad (2) \end{aligned}$$

Generally, in the presence of multipath, the transfer function phase in (1) is a nonlinear function of frequency. If the amplitude of secondary multipath components is small, the first term in (1) will be the dominant component. In that case, all terms

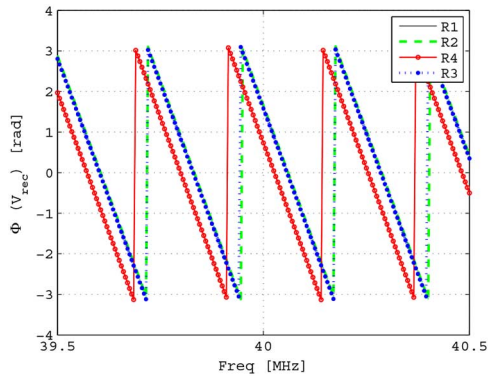


Fig. 2. Phase variation in the received signal as a function of frequency for the four Rx positions R_1 – R_4 as shown in Fig. 1, computed via an FDTD full-wave electromagnetic simulation of the scene.

$k \geq 1$ in (1) can be ignored, and only the leading term in the numerator and denominator of (3) will be significant, resulting in a phase that is linear in frequency given by $\phi - 2\pi f n_0$. In Fig. 2, the phase of the received signal at each received antenna position is plotted against frequency, centered around 40 MHz. The linear phase variation (aside from phase wrapping) in the bandwidth of interest is evidence of the minimal effect of multipath in this scenario. Similar results (not shown) occur in the transfer function amplitude, which is flat across the simulated bandwidth. Although there is attenuation due to penetration, there is little evidence of multipath propagation or fading. For example, in the case of Rx position R_2 , there are four layers of walls between the transmit antenna which is outside the building and the Rx located indoors. The received signal is predominantly the component that penetrates through the walls along the shortest path between the Tx and Rx antennas. Reflections and multiple scattering between walls are very small due to the small size of the walls (note that the thickness of a typical wall is a small fraction of the wavelength at 40 MHz).

III. MEASUREMENTS AND PROCESSING

A. Measurement System and Scenarios

To efficiently conduct large-scale experiments, we integrated a universal radio software peripheral (USRP) Rx system and a $\lambda/6$ short dipole antenna onto a robotic platform which is tele-operated throughout the measurement scenarios, enabling data collection over extended indoor/outdoor environments (e.g., see Scenario 3 in Section III). By integrating the USRP with the robot control system, each radio measurement is automatically supplemented with time and position information. The measurement system diagram is given in Fig. 3. A detailed description of the measurement system can be found in [22].

Measurements were carried out in three different environments, two indoor (Scenarios 1 and 2) and one extended indoor/outdoor (Scenario 3). Different cases are listed in Table I and experimental parameters are shown in Table II. The Tx and Rx positions in Table II correspond to those marked in Figs. 4 through 6, as described next.

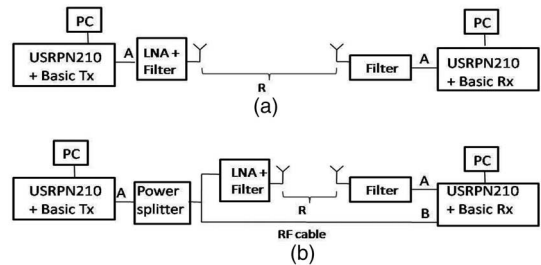


Fig. 3. USRP-based one-way (dual channel) measurement system diagrams for: (a) pulse and packet tests and (b) tone tests. The pulse and packet tests are used to characterize the channel phase distortion and BER, respectively. For the tone test, a reference channel is introduced by cable connection, allowing direct comparison of the wireless and wired signals.

TABLE I
MEASUREMENT SCENARIOS INDICATING TRANSMIT LOCATIONS AND RX REGIONS, WITH REFERENCE TO FIGS. 4–6, RESPECTIVELY

	Environment	Tx position	Rx locations	Setup
Case 1a	Scenario 1	P_1	P_3 – P_6	NLoS
Case 1b	Scenario 1	P_1	P_7 – P_{13}	NLoS
Case 1c	Scenario 1	P_1	P_3	NLoS
Case 2a	Scenario 1	P_2	P_3 – P_5	NLoS
Case 2b	Scenario 1	P_0	P_1	LoS
Case 3a	Scenario 2	P_1	P_2 – P_7	LoS
Case 3b	Scenario 2	P_1	P_6 – P_7	LoS
Case 3c	Scenario 2	P_1	P_7 – P_{11}	NLoS
Case 3d	Scenario 2	P_1	P_8 – P_9	NLoS
Case 4	Scenario 2	P_0	P_{12} – P_{16}	NLoS
Case 5a	Scenario 3	P_0	R_0	NLoS
Case 5b	Scenario 3	P_1	R_4 – R_7	NLoS
Case 5c	Scenario 3	P_0	R_8, R_9	NLoS
Case 5d	Scenario 3	P_1	R_1 – R_3	NLoS
Case 5e	Scenario 3	P_0	R_8, R_9	NLoS

Most measurements consisted of NLoS propagation.

TABLE II
PARAMETERS USED FOR MEASUREMENTS

Parameter	Setting
Max. Tx power	15 dBm (32 mW)
Tx, Rx ant. gain	–6.5 dBi, –6.5 dBi
Tx ant. height	1 m (0.13 λ)
Rx ant. height	0.8 m, 1 m (0.1 λ)
Tx, Rx pol.	V, V
Tx amp. gain	40 dB

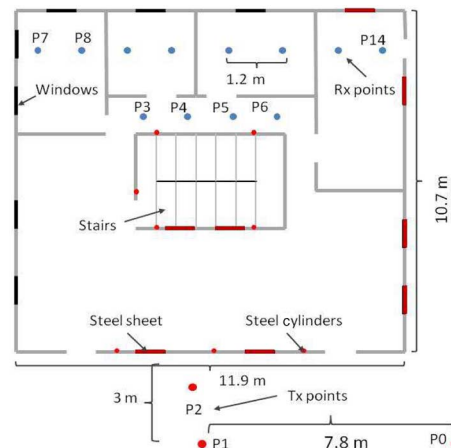


Fig. 4. Measurement Scenario 1: second floor layout of wooden building, with steel sheets and cylinders introduced as shown.

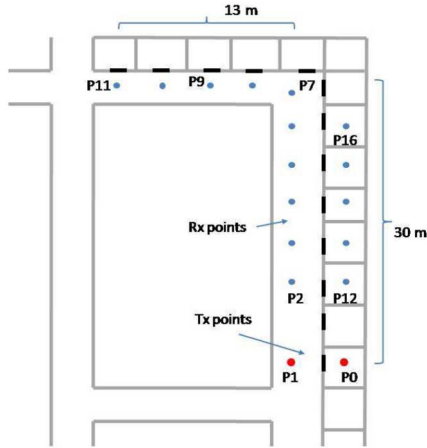


Fig. 5. Measurement Scenario 2: L-shaped corridor in the second floor of a much larger office and laboratory building with substantial metallic partitions and walls.



Fig. 6. Measurement Scenario 3: overhead view of the test facility. P_0 and P_1 are the two Tx positions and R_0 to R_9 are various indoor and outdoor regions traversed by the robot for data collection.

Scenario 1 consists of indoor measurements in a multi-story house-like test facility. Fig. 4 shows a schematic of the first floor of this building that has the same geometry as the one simulated (see Fig. 1 in Section II). This is a wooden structure, including the floors, walls, and ceilings. As indicated in Fig. 4, steel cylinders and sheets were inserted as might occur in a home environment. Scenario 2 is depicted in Fig. 5, interior to an office and laboratory building with extensive metal partitions, reinforced walls, and metal objects. Measurements were taken in the hallways, adjacent to offices and large interior lab bays. Measurements in Scenarios 1 and 2 were taken up to a maximum range of 40 m, in LoS and nonLoS (NLoS) conditions. For Scenario 3, the test facility shown in Fig. 6 was utilized, with a test diameter of about 200 m, consisting of multiple buildings constructed of concrete and cinderblock, with fences and other dielectric and metallic objects in the scene. Thousands

of measurements were collected for the two different Tx positions denoted P_0 and P_1 in the figure, teleoperating the mobile robotic collection platform within the denoted oval collection regions and along the dashed-line collection path shown.

B. Pulse Tests

In this section, we describe our pulse-based test for the presence of phase distortion. These experiments are based on periodically transmitting root-raised cosine (RRC) pulses, a ubiquitous waveform used in digital communications [23].

1) *Pulse Test Parameters:* Let $p(n)$ denote the discrete-time RRC pulse. Referring to the RRC formula in [23], $p(t)$ has roll-off factor $\beta = 0.9$, symbol time $T_S = 3.2 \times 10^{-5}$ s, and pulse duration 1.28×10^{-4} s. We transmit a periodic pulse train with 8.72×10^{-4} s off-time between pulses during which null samples are fed to the DAC. We transmit in both the in-phase (I) and quadrature (Q) channels, denoting the complex baseband equivalent as $p_c(t) = p(t) + jp(t)$. The RRC pulse has 10 dB bandwidth of approximately 60 kHz.

In our tests, the Tx location is fixed and the pulse train is continuously emitted. The Rx, mounted on a robot, is navigated to a given point and stopped. For each unique Rx position, 125 pulses are collected, corresponding to $\frac{1}{8}$ s of collection time and denote the received signal $p_T(n)$. After sampling, the resulting digital signal at complex baseband is denoted by $r(n) = p_T(n) * h(n) + b(n)$, where $h(n)$ is the channel impulse response, and $b(n)$ is assumed to be an AWGN random process. In the analysis that follows, we assume that all 125 pulses collected at a fixed point propagate through an identical channel.

The received complex baseband pulse train $r(n)$ is passed through a matched filter (MF) whose template is the RRC pulse shape. Denoted by p_M , the output of match filtering $p_c(n)$ against $p(n)$; note that $p_M(n)$ is a complex valued signal with equal I and Q channels. We then estimate timing and compute the average of the MF individual pulse responses, given by $p_R(n) = \frac{1}{125} \sum_{i=1}^{125} p_{M,i}(n)$, where $p_{M,i}(n)$ denotes the MF response to the i_{th} received pulse. Given the RRC pulse shape, $p_{M,i}(n)$ is ideally a raised cosine shape, if there were no noise or channel distortion. The additive noise effect is minimized by averaging the individual MF responses.

To test for deviation from an ideal channel without multipath, we compute the observed channel transfer function given by $H_R = \frac{\mathcal{F}(p_R)}{\mathcal{F}(p_M)}$, where \mathcal{F} denotes the discrete Fourier transform (computed via an FFT algorithm). Here, $\mathcal{F}(p_R)$ is the DFT of the measured averaged received pulse after matched filtering, and $\mathcal{F}(p_M)$ is the DFT of the ideal MF response (a raised cosine pulse). Without multipath, the LTI channel consists of scaling and a single delay only, as discussed in Section II. We normalize the initial delay to zero, and the maximum transfer function amplitude to unity, so that ideally $|H_R| = 1$ with phase equal to zero.

Multipath propagation induces frequency-dependent deviations from the ideal transfer function in both magnitude and phase, so we consider two measures of channel distortion. Let S denote the selected set of frequencies under test, taken from

the DFT. We define a mean-square error (MSE) of the difference between the measured and ideal unity magnitude response given by

$$M = \frac{1}{|S|} \sum_{f \in S} [|H_R(f)| - 1]^2. \quad (3)$$

The MSE of the difference between the measured channel phase response and its ideal zero value is given by

$$P = \frac{1}{|S|} \sum_{f \in S} [\angle H_R(f)]^2. \quad (4)$$

These two measures, sample averages computed across the DFT frequency bin set S , capture the discrepancy of the measured channel H_R from an idealized all-pass, zero-phase filter. Note that for each fixed transmit-receive location, there is a single channel realization H_R , and hence one value for M and one for P for each experimental Rx position. Small values for P provide evidence of minimal phase distortion, and small values for M are indicative of a constant attenuation with respect to frequencies probed by the pulse.

2) *Wider Bandwidth Pulse Tests*: The transmit pulse bandwidth can easily be increased or decreased in the software-defined radio Tx by changing the sampling rate when generating the RRC waveform. In addition to the above case, we also generated an RRC pulse stream with symbol duration of $T_S = 1.935 \times 10^{-6}$ with single pulse duration of 7.74×10^{-6} s. In this case, we transmit 10 000 pulses/s, so that the total time between two consecutive pulse starts is $T = 10^{-4}$ s. The RRC pulse has 3-dB bandwidth of approximately 500 kHz and 10-dB bandwidth of 800 kHz.

C. Tone Tests

A second phase distortion analysis technique is also pursued, which is based on tones transmitted simultaneously over the air and via a cabled reference channel, shown in Fig. 3(b). These tests were conducted by moving the Rx to each new Rx location. Tone frequencies are selected within [39.5, 40.5] MHz. The transmit signal is divided between the antenna and an SMA cable (reference) using a power divider. Likewise at the Rx, complex baseband samples of the two separate signals are acquired simultaneously from the two channels which are controlled by the same clock. For a given frequency, the instantaneous received phase is computed for both the antenna signal and the reference. The difference in instantaneous phase, averaged over all samples collected at a given frequency f , yields our estimate of the phase response at f .

IV. EXPERIMENTAL RESULTS

A. Path-Loss

We first report on the path-loss observed in Scenario 3. We utilize the pulse data described in Section III-B, for case 5a in Table I (outdoor, NLoS). For each fixed Rx location, in-phase (I) and quadrature (Q) samples are collected spanning 125 pulses, which are used to compute raw pulse power (P_r^{uncal}) that needs to be calibrated because the I and Q samples do

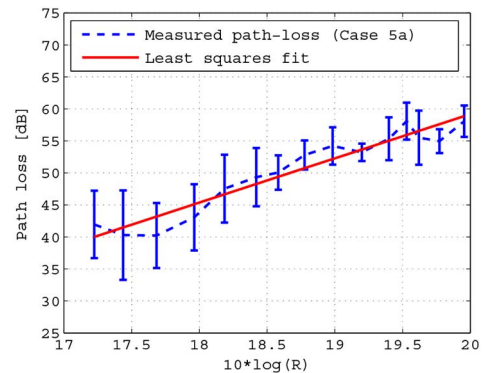


Fig. 7. Mean (dashed line) and standard deviation (solid vertical bars) of measured path-loss in Scenario 3 (Fig. 6 Case 5a in Table I). The solid line is the least squares fit.

not map linearly to the actual receive power. Simultaneously, we also store GPS location information. The GPS data are postprocessed to enhance the accuracy by leveraging the auxiliary sensors of the robot, including inertial measurement unit (IMU), laser scanner, and odometry by using measured ground truth and Google Maps as a reference.

To calculate the path-loss at a fixed location, the out-of-band noise is reduced with a narrowband bandpass filter. Next, P_r^{uncal} is computed by finding the peak value of $|P_c(n)|^2$ (the “peak power”) for each pulse in the pulse train received at that location, and then averaging across all these peak power values. Then, the channel path-loss (in dB) is computed using

$$PL = P_t - P_r^{\text{uncal}} + G_t + G_r + G_{sys} \quad (5)$$

where P_t and P_r^{uncal} are the transmit and receive powers in dBm, respectively. Here, G_t and G_r are the gains of the Tx and Rx antennas, and G_{sys} is the sum of all other system gains and losses including amplifier gain, filter loss, and cable losses. G_{sys} also includes a calibration factor for the USRP to map I and Q values to true power levels. This calibration factor was computed by directly connecting the USRP to a signal generator via an RF cable and performing a power sweep to map the quantity captured by P_r^{uncal} to actual signal power in dBm. Next, the corrected GPS data are used to find the distance between the Rx and Tx for all measurement points. The range data are binned into intervals of size 0.45λ (chosen to be similar to the position error of our system), with the path-loss data mapped to its corresponding bin, and the mean and standard deviation of all path-loss values falling in a given bin are computed. The overall position error attributable to our measurement system is within ± 1.5 m, which comes from errors in the GPS data and simultaneous localization and mapping (SLAM) processing. It should be noted that the linear path-loss trend does not change when the bin size is reduced, although the path-loss curve will not be as smooth and has a slight increase in standard deviation.

The path-loss mean and standard deviation versus range is shown in Fig. 7, which is based on measurements in Scenario 3 (case 5a) and consists of a total of 152 collection points. The path-loss for this case has a standard deviation of 2 dB from the least squares fit. The calculated path-loss exponent is 6.3. This path-loss exponent value is slightly higher than typical

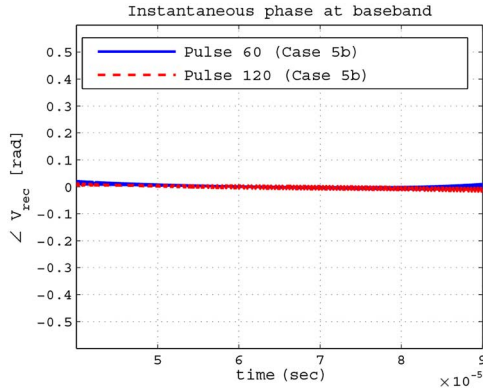


Fig. 8. Instantaneous phase versus time for two example complex baseband received pulses after frequency offset correction, for a Rx position selected from case 5 b (see Fig. 6 and Table I). Little phase distortion is evident for high SNR cases such as these.

indoor/outdoor path-loss exponent values reported in the literature for the upper VHF, UHF, and microwave range (roughly 4–6.5) [24].

In the lower VHF with low antenna heights ($\leq 0.5\lambda$), propagation is primarily supported by surface waves, resulting in the higher path-loss exponent value because surface waves decay faster in general [19], [25]. Note, however, that while the path-loss exponent is relatively high, the overall attenuation is much less than expected at higher frequencies due to lower penetration loss through the walls [18]. It should also be noted that other measurements in Scenario 3 (with different Tx locations) have resulted in path-loss exponent values ranging from 4 to 5 (partly due to the lower antenna heights). The path-loss variation depends on the number of obstacles and buildings in the path. Our reported measurements in Scenario 3 are a challenging case with a significant number of structures in the typical LoS path. A more extensive measurement-based path-loss characterization for VHF indoor/outdoor channels, as well as comparison against measurements at 2.4 GHz, is presented in [18]. Although the measurements were carried out in different indoor and outdoor scenarios, the path-loss results presented in [18] are comparable to the path-loss results discussed in this paper.

B. Phase Distortion and Instantaneous Phase

Multipath or other propagation effects can generally introduce phase distortion. To look more closely at this, we examine the instantaneous phase for two representative pulse cases. In Fig. 8, we plot instantaneous phase against time, for two complex baseband pulses from Scenario 3 case 5b, Rx location R_6 (see Table I and Fig. 6). The instantaneous phase plotted in Fig. 8 consists of the middle 1250 samples of the received pulse, out of 3200 samples per pulse. Rx processing consisted of band-pass filtering to reduce out of band noise, passband sampling, frequency offset estimation, and mixing to complex baseband. No MF processing or averaging was used. The plots represent arbitrarily chosen 60th and 120th pulses of the 125 collected at this particular Rx position, and the SNR was measured to be close to 20 dB for each pulse. In fact, the entire ensemble of 125 pulses all show the same instantaneous phase as in Fig. 8.

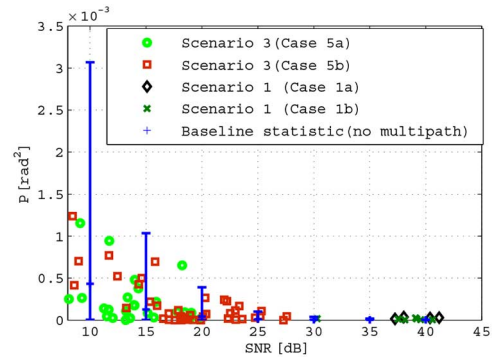


Fig. 9. Mean square deviation of the received signal phase compared with an ideal channel transfer function for cases 5a and 5b (see Fig. 6 and Table I). P measures deviation from the ideal zero channel transfer function phase. Little statistical deviation is observed at the 95% level.

Note that quadrature results in a constant noise-free pulse phase of $\pi/4$, which has been removed for plotting. Also, carrier frequency offset error will result in a linear phase change with time; we estimate and remove this linear trend before plotting.

After removing the $\pi/4$ offset and linear trend due to carrier offset, plots of instantaneous phase display remarkably little variation from zero for these and all other high SNR cases examined, demonstrating very little observed phase distortion. The slight variation in the phase plots is well within what can be expected due to the inherent limitations of our measurement system.

C. Statistical Analysis of the Measured Channel Transfer Function

Next, we report on the measured statistics of the channel transfer function as described in Section III-B, using the error measures M and P from (3) and (4), respectively. To establish baseline distributions for M and P for each fixed SNR, we simulate a channel which introduces only attenuation and AWGN (an ideal all-pass zero-phase transfer function). We perform the identical transmit and receive data generation and processing that we do in our actual data collection based on processing a pulse train, as was described in Section III-B. For each SNR value, we conducted 500 Monte Carlo trials over realizations of the additive noise. We used the resulting empirical distributions of M and P to find a lower $1 - \alpha$ confidence interval for each, i.e., we find threshold values τ_M and τ_P , such that $\Pr(M > \tau_M) = \alpha$ and $\Pr(P > \tau_P) = \alpha$. Note that these threshold values are a function of the test SNR. For our tests, we use $\alpha = .05$ to yield a 95% confidence level.

Figs. 9 and 10 depict experimental results for measurements carried out in Scenario 3 and Scenario 1. These results consist of 11 and 97 different Rx positions in Scenario 1 and Scenario 3, respectively. The data collected at each measurement point consist of 250 pulses in the case of Scenario 1 and 125 pulses in the case of Scenario 3 resulting in a total of 14 875 measured pulses. For each SNR, the intervals $(0, \tau_M)$ and $(0, \tau_P)$ are also shown as vertical blue bars. Note that in Fig. 10, these bars have a slight upward bias from their ideal lower end point of 0. This is attributable to a small departure from unity gain due to roll-off in the magnitude response of the

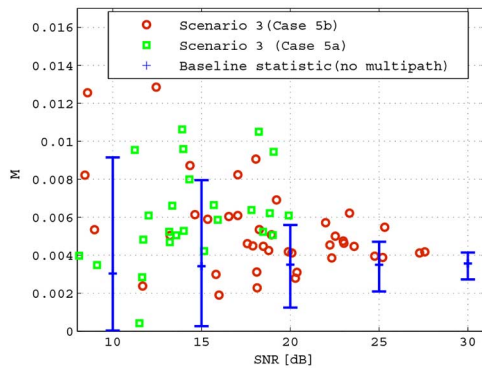


Fig. 10. Mean square deviation of the received signal amplitude compared with an channel transfer function for cases 5a and 5b (see Fig. 6 and Table I). M measures deviation from the ideal unity gain transfer function amplitude. Only a small deviation is observed.

lowpass filter used in processing the pulses. Statistical evidence of deviation from the ideal transfer function exists at level α if, for a particular computed value, $M > \tau_M$ or $P > \tau_P$.

The phase statistic P in Fig. 9 shows that all the Rx positions considered resulted in a channel transfer function whose phase deviation from an ideal delay and attenuation channel is well within statistical limits caused by additive noise. We cannot reject the ideal transfer function model at the $\alpha = .01$ level. The amplitude statistic shown in Fig. 10 shows similar results, with most measurements within the statistical limits, although there is some deviation. However, this statistical deviation is small, and appears to be independent of the phase results. A more refined analysis could consider the joint distribution of M and P , although only a small variation in attenuation is observed, and the transfer function phase seems more pertinent to the measurement of phase distortion.

The phase and amplitude statistics are also computed for the wideband pulse tests described in Section III-B. Fig. 11 shows the phase statistic calculated based on measurements carried out in Scenario 2 where a few LoS and NLoS points were measured. Similar to the previous case, the phase deviation in two of the three cases falls within the 95% confidence intervals of the null hypothesis; the third is just slightly outside it. In this figure, we also show the theoretical phase MSE for various two-component multipath channels, i.e., channels consisting of a dominant component and a single multipath component. We show channels whose secondary component has energy that is a fraction α of the dominant signal, and delay of γ meters relative to the dominant signal, for various values of α and γ (as shown in the figure legend). For example, the point $\alpha = .05$, $\gamma = 10$ represents the phase deviation statistic value we would obtain for a two component multipath channel, whose secondary component is .05 as strong as the primary one, and which travels an excess distance (in free space) of 10 m. Note that for the higher SNR cases, most multipath channels give phase MSE values which fall outside the null hypothesis interval; this indicates that the test has strong statistical power. Also, note that in general, as the secondary component's relative energy and/or delay increases, the value of the statistic grows, i.e., that P grows larger as multipath becomes "worse." Finally, note that the various multipath channel statistics are point estimates computed without AWGN; with AWGN, the points would become

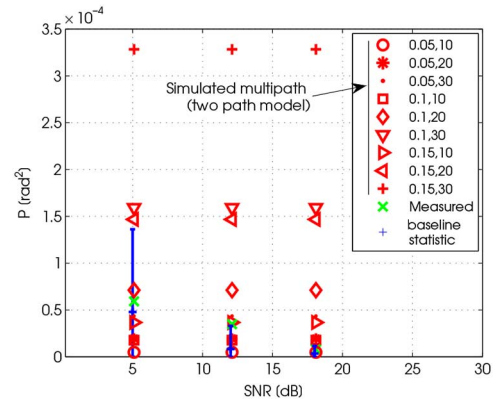


Fig. 11. Mean square deviation of the measured phase for case 3d (see Fig. 6 and Table I), along with various realizations of theoretical multipath channels based on a two-path channel model. The first and second numbers in the legends of the theoretical multipath points are the normalized amplitude and delay of the secondary (multipath) component with respect to the dominant component. Dominant component is normalized to have energy 1 and delay 0. A 95% confidence interval for the distribution of the phase statistic under an ideal flat fading channel with AWGN is shown (blue bar). Note that actually obtained experimental values (green x) fall within or very near the blue bar.

intervals and would shift strictly up. We have not shown these latter intervals, so as not to clutter the figure.

The amplitude statistic shows qualitatively similar results; however, the Tx and Rx antennas exhibit small amplitude variations (i.e., are not constant gain) over the pulse bandwidth which affects our magnitude MSE statistic. Note that this is more of an issue for the wider bandwidth pulses than the narrow bandwidth pulses, as the larger bandwidth results in a larger overall deviation from constant gain. The net effect of this system nonideality is to add noise to our magnitude MSE statistic. Rather than carefully compensate for the effect of this antenna gain variation on our magnitude statistic, we have focused on the phase statistic.

D. Tone Tests for Transfer Function Phase Measurement

Next, we present results for tone tests as described in Section III-C, where we measure the phase difference between the received tone via the antenna and via the cabled reference channel. An experimental result is plotted in Fig. 12. Other measured cases also show similar linear variation and can be found in [22]. The curve shows the result for NLoS case collected in Scenario 1, shown in Fig. 4. At each measurement location, we collect 1 s of complex-valued data at 2 MS/s from the two channels for each frequency. The phase difference is calculated for each sample, and the mean and standard deviation of the phase difference is plotted.

The experimental results show a linear phase as a function of frequency for the entire range of test tones in [39.5, 40.5] MHz, which is consistent with an ideal unity transfer function over the frequencies tested. Some deviation is expected due to varying SNR and other experimental effects, but the measured deviation is small as shown in the figures. We note that multipath will become evident as the frequency is increased, even within the VHF band. In a previous publication, the authors have investigated the propagation characteristics at HF/lower VHF as compared to 100 MHz and higher, using full-wave

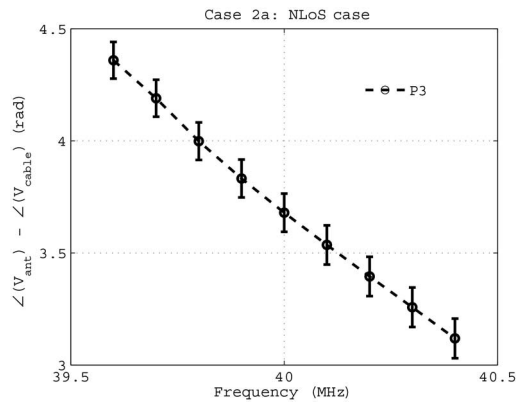


Fig. 12. Tone tests: mean and standard deviation of the measured phase difference between the wireless and reference channels for case 2a, at Rx point P3 (see Fig. 4 and Table I).

simulations [3]. For a given indoor building scenario, the effect of multipath and channel induced distortion is clearly evident at 100 MHz, but is very minimal at lower frequencies such as 20 or 40 MHz. This is easily seen in the amplitude and phase maps inside the building [3].

V. CONCLUSION

In this paper, we have characterized the lower VHF channel near 40 MHz in highly cluttered environments using an extensive measurement campaign and statistical analysis. Our objective was to study the viability of low power, short range, reliable communications that are minimally affected by the presence of clutter, and to establish the degree to which phase distortion is present. FDTD electromagnetic simulations of an indoor/outdoor scene showed little phase distortion or multipath propagation that is characteristic of upper VHF and above. Tone and pulse-based measurements were conducted in various indoor/outdoor scenarios, including NLoS cases, at ranges up to 200 m. It was shown through various techniques that the channel phase distortion and multipath are minimal in all tested scenarios.

In summary, our central finding is that for low power, short-range low-data rate communications in the variety of cluttered indoor/outdoor environments tested, the lower VHF channel can be reasonably modeled as an AWGN channel with scalar attenuation. The simplicity of the channel, along with recent advances in the design of extremely miniaturized lower VHF antennas, can be exploited in a large variety of signal processing and communication applications such as geolocation in GPS-denied environments and voice communications in search-and-rescue operations.

ACKNOWLEDGMENT

The authors would like to thank J. N. Twigg, J. M. Gregory, Dr. E. Stamp, Dr. J. Rodgers, and S. H. Young of the Army Research Laboratory for their support with robotic integration and experiments. They would also like to thank J. Choi of the University of Michigan for help with the fabrication of the antennas utilized in this work.

REFERENCES

- [1] J. R. Hampton *et al.*, "Urban propagation measurements for ground based communication in the military UHF band," *IEEE Trans. Antennas Propag.*, vol. 54, no. 2, pp. 644–654, Feb. 2006.
- [2] J. Andrusenko *et al.*, "VHF general urban path loss model for short range ground-to-ground communications," *IEEE Trans. Antennas Propag.*, vol. 56, no. 10, pp. 3302–3310, Oct. 2008.
- [3] F. T. Dagefu, J. Oh, and K. Sarabandi, "A sub-wavelength RF source tracking system for GPS-denied environments," *IEEE Trans. Antennas Propag.*, vol. 61, no. 4, pp. 2252–2262, Apr. 2013.
- [4] F. T. Dagefu, J. Oh, J. Choi, and K. Sarabandi, "Measurements and physics-based analysis of co-located antenna pattern diversity system," *IEEE Trans. Antennas Propag.*, vol. 61, no. 11, pp. 5724–5734, Nov. 2013.
- [5] W. T. Barnett, "Multipath propagation at 4, 6, 11 GHz," *Bell Syst. Tech. J.*, vol. 51, no. 2, pp. 321–361, Feb. 1972.
- [6] C. L. Ruthroff, "Multiple-path fading on line-of-sight microwave radio systems as a function of path length and frequency," *Bell Syst. Tech. J.*, vol. 50, no. 7, pp. 2375–2398, Sep. 1971.
- [7] B. M. Sadler and A. Swami, "On the performance of episodic UWB and direct-sequence communication systems," *IEEE Trans. Wireless Commun.*, vol. 3, no. 6, pp. 2246–2255, Nov. 2004.
- [8] Y. Alvarez, F. Las-Heras, and M. R. Pino, "Full-wave method for RF sources location," in *Proc. IEEE 2nd Eur. Conf. Antennas Propag. (EuCAP'07)*, 2007, pp. 1–5.
- [9] J. Oh, J. Choi, F. T. Dagefu, and Kamal Sarabandi, "Extremely small two-element monopole antenna for HF band applications," *IEEE Trans. Antennas Propag.*, vol. 61, no. 6, pp. 2991–2999, Jun. 2013.
- [10] J. Oh and K. Sarabandi, "A moderate gain extremely short HF monopole antenna," in *Proc. IEEE 6th Eur. Conf. Antennas Propag. (EuCAP'12)*, 2012, pp. 1657–1660.
- [11] [Online]. Available: <http://transition.fcc.gov/oet/spectrum/table/fcctable.pdf>
- [12] T. S. Rappaport, "Characterization of UHF multipath radio channels in factory buildings," *IEEE Trans. Antennas Propag.*, vol. 37, no. 8, pp. 1058–1069, Aug. 1989.
- [13] C. Perez-Vega and J. M. Zamanillo, "Path-loss model for broadcasting applications and outdoor communication systems in the VHF and UHF bands," *IEEE Trans. Broadcast.*, vol. 48, no. 2, pp. 91–96, Jun. 2002.
- [14] G. B. Rowe, A. G. Williamson, and B. Egan, "Mobile radio propagation in Auckland at 76 MHz," *IEEE Electron. Lett.*, vol. 19, no. 25, pp. 1064–1065, Dec. 1983.
- [15] J. A. Pugh and P. J. Vigneron, "Propagation models for mobile terrestrial VHF communications," in *Proc. IEEE Mil. Commun. Conf. (MILCOM)*, San Diego, CA, USA, 2008, pp. 1–7.
- [16] Y. Okumura, E. Ohmori, T. Kawano, and K. Fukuda, "Field strength and its variability in the VHF and UHF land-mobile radio service," *Rev. Elect. Commun. Lab.*, vol. 16, no. 9–10, pp. 828, Sep./Oct. 1968.
- [17] M. Hatay, "Empirical formula for propagation loss in land mobile radio services," *IEEE Trans. Veh. Technol.*, vol. 29, no. 3, pp. 317–325, Aug. 1980.
- [18] F. T. Dagefu, J. Choi, M. Sheikhsofla, B. M. Sadler, and K. Sarabandi, "Performance assessment of lower VHF band for short range communication and geolocation applications," *Radio Sci. J.*, vol. 50, pp. 1–10, doi: 10.1002/2014RS005601, to be published.
- [19] F. T. Dagefu and K. Sarabandi, "Analysis and modeling of near-ground wave propagation in the presence of building walls," *IEEE Trans. Antennas Propag.*, vol. 59, no. 6, pp. 2368–2378, Jun. 2011.
- [20] C. Watterson, J. Juroshek, and W. D. Bensema, "Experimental confirmation of an HF channel model," *IEEE Trans. Commun. Technol.*, vol. 18, no. 6, pp. 792–803, Dec. 1970.
- [21] EMAG Technologies Inc. [Online]. Available: <http://www.Emagware.com>
- [22] F. T. Dagefu *et al.*, "Low VHF channel measurements and simulations in indoor and outdoor scenarios," U.S. Army Research Laboratory, Tech. Rep. ARL-TR-7282, May 2015.
- [23] J. Proakis, *Digital Communications*, 3rd ed. New York, NY, USA: McGraw Hill, 1995.
- [24] X. Zhang, T. W. Burrell, K. B. Albers, and W. B. Kuhn, "Propagation comparisons at VHF and UHF frequencies," in *Proc. IEEE Radio Wireless Symp.*, 2009, pp. 244–247.
- [25] D. Liao and K. Sarabandi, "Near-earth wave propagation characteristics of electric dipole in presence of vegetation or snow layer," *IEEE Trans. Antennas Propag.*, vol. 53, no. 11, pp. 3747–3756, Nov. 2005.



Fikadu T Dagefu (S'07–M'12) received the B.S. degree from the University of Texas, Austin, TX, USA, in 2007, and the M.S. and Ph.D degrees from the University of Michigan, Ann Arbor, MI, USA, in 2009 and 2012, all in electrical engineering.

He is currently a Postdoctoral Fellow with the U.S. Army Research Laboratory (ARL), Adelphi, MD, USA. His research interests include physics-based channel modeling and measurements, geolocation in GPS-denied environments, low-VHF networking, and hybrid multiwavelength systems.

Dr. Dagefu was the recipient of the 2011 MIT Lincoln Laboratory Graduate Fellowship. He is a member of Eta Kappa Nu and Tau Beta Pi honor societies. He was a Finalist in the student paper competitions at the IEEE IGARSS International Conference in 2009 and 2010.



Gunjan Verma received the B.S. degree in mathematics, the B.S. degree in computer science, and the B.A. degree in economics from Rutgers University, New Brunswick, NJ, USA, and the M.S. degree in applied mathematics from Johns Hopkins University, Baltimore, MD, USA.

He is with the U.S. Army Research Laboratory (ARL), Adelphi, MD, USA. His research interests include information flow in complex networks, signal processing, and validation and prototyping of wireless communications algorithms using software-

defined radios.



Chirag R. Rao received the B.S. degree in electrical and computer engineering from Cornell University, Ithaca, NY, USA, in 2013.

He is currently with the U.S. Army Research Laboratory, Adelphi, MD, USA. His research interests include wireless network communication, autonomous systems, and information science.



Paul L. Yu (S'08–M'09) received the B.S. degree in mathematics, the B.S. degree in computer engineering, and the Ph.D. degree in electrical engineering from University of Maryland, College Park, MD, USA, in 2002, 2003, and 2008, respectively.

He is with the U.S. Army Research Laboratory (ARL), Adelphi, MD, USA. His research interests include areas of signal processing, wireless communications, and network science. His most recent work focuses on the exploitation of mobility for improved wireless network connectivity in complex propaga-

tion environments.



Jonathan R. Fink (S'04–M'11) received the B.S. degree in electrical and computer systems engineering from Rensselaer Polytechnic Institute, Troy, NY, USA, in 2004, and the Ph.D. degree in electrical and systems engineering from the University of Pennsylvania, Philadelphia, PA, USA, in 2011.

He is a Research Scientist with the U.S. Army Research Laboratory, Adelphi, MD, USA. His research interests include collaboration and planning for multi-robot systems with emphasis on communication modeling and planning for network

connectivity.



Brian M. Sadler (S'81–M'81–SM'02–F'07) received the B.S. and M.S. degrees from the University of Maryland, College Park, MD, USA, and the Ph.D. degree from the University of Virginia, Charlottesville, VA, USA, all in electrical engineering.

He is a Fellow of the Army Research Laboratory (ARL), Adelphi, MD, USA. His research interests include information science, networked and autonomous systems, sensing, and mixed-signal integrated circuit architectures.

Dr. Sadler is an Associate Editor for *EURASIP Signal Processing*, was an Associate Editor for the *IEEE TRANSACTIONS ON SIGNAL PROCESSING* and *IEEE SIGNAL PROCESSING LETTERS*, and has been a Guest Editor for several journals including *IEEE JSTSP*, *IEEE JSAC*, the *IEEE SP Magazine*, and the *International Journal of Robotics Research*. He is a member of the IEEE Signal Processing Society Sensor Array and Multi-channel Technical Committee, and Co-Chair of the IEEE Robotics and Automation Society Technical Committee on Networked Robotics. He was the recipient of the Best Paper Awards from the Signal Processing Society in 2006 and 2010, several ARL and Army R&D Awards, as well as a 2008 Outstanding Invention of the Year Award from the University of Maryland.



Kamal Sarabandi (S'87–M'90–SM'92–F'00) received the B.S. degree in electrical engineering from Sharif University of Technology, Tehran, Iran, in 1980, dual M.S. degrees in electrical engineering and mathematics, and the Ph.D. degree in electrical engineering from the University of Michigan, Ann Arbor, MI, USA, in 1986, 1989, and 1989, respectively.

He is currently the Director of the Radiation Laboratory and the Rufus S. Teesdale Professor of Engineering with the Department of Electrical

Engineering and Computer Science, University of Michigan, Ann Arbor, MI, USA. He possesses 25 years of experience with wave propagation in random media, communication channel modeling, microwave sensors, and radar systems and leads a large research group including two research scientists and 16 Ph.D. students. He has graduated 40 Ph.D. and supervised numerous post-doctoral students. He has served as the Principal Investigator on many projects sponsored by the National Aeronautics and Space Administration (NASA), Jet Propulsion Laboratory (JPL), Army Research Office (ARO), Office of Naval Research (ONR), Army Research Laboratory (ARL), National Science Foundation (NSF), Defense Advanced Research Projects Agency (DARPA), and a large number of industries. He is currently leading the Center for Microelectronics and Sensors funded by the Army Research Laboratory under the Micro-Autonomous Systems and Technology (MAST) Collaborative Technology Alliance (CTA) program. He has authored many book chapters and more than 220 papers in refereed journals on miniaturized and on-chip antennas, meta-materials, electromagnetic scattering, wireless channel modeling, random media modeling, microwave measurement techniques, radar calibration, inverse scattering problems, and microwave sensors. He has also had more than 500 papers and invited presentations in many national and international conferences and symposia on similar subjects. His research interests include microwave and millimeter-wave radar remote sensing, meta-materials, electromagnetic wave propagation, and antenna miniaturization.

Dr. Sarabandi served as a member of the NASA Advisory Council appointed by the NASA Administrator for two consecutive terms from 2006 to 2010. He is serving as a Vice President of the IEEE Geoscience and Remote Sensing Society (GRSS) and is a Member of the Editorial Board of the *PROCEEDINGS OF THE IEEE*. He was an Associate Editor of the *IEEE TRANSACTIONS ON ANTENNAS AND PROPAGATION* and the *IEEE SENSORS JOURNAL*. He is a member of Commissions F and D of URSI. He was the recipient of the Henry Russel Award from the Regent of the University of Michigan, the GAAC Distinguished Lecturer Award from the German Federal Ministry for Education, Science, and Technology in 1999, the 1996 EECS Department Teaching Excellence Award, the 2004 College of Engineering Research Excellence Award, the IEEE GRSS Distinguished Achievement Award and the University of Michigan Faculty Recognition Award in 2005, the Best Paper Award at the 2006 Army Science Conference, the Humboldt Research Award from The Alexander von Humboldt Foundation of Germany, in 2008, and the Best Paper Award at the IEEE Geoscience and Remote Sensing Symposium, and the 2010 Distinguished Faculty Achievement Award from the University of Michigan. The IEEE Board of Directors announced him as the recipient of the 2011 IEEE Judith A. Resnik Medal. In the past several years, joint papers presented by his students at a number of international symposia (IEEE APS'95,'97,'00,'01,'03,'05,'06,'07; IEEE IGARSS'99,'02,'07,'11; IEEE IMS'01; USNC URSI'04,'05,'06,'10,'11; AMTA'06; URSI GA 2008) have received best paper awards.